Broadband non-reciprocity with robust signal integrity in a triangle-shaped

nonlinear 1D metamaterial

Lezheng Fang, Amir Darabi, Alireza Mojahed, Alexander F. Vakakis, Michael J. Leamy*

Abstract

In this paper we propose and numerically study a nonlinear, asymmetric, passive metamaterial

that achieves giant non-reciprocity with i) broadband frequency operation and ii) robust signal

integrity. Previous studies have shown that nonlinearity and geometric asymmetry are necessary

to break reciprocity passively. Herein, we employ strongly nonlinear coupling, triangle-shaped

asymmetric cell topology, and spatial periodicity to break reciprocity with minimal frequency

distortion. To investigate the nonlinear band structure of this system, we propose a new

representation, namely, a wavenumber-frequency-amplitude band structure, where amplitude-

dependent dispersion is quantitatively computed and analyzed. Additionally, we observe and

document the new nonlinear phenomenon of time-delayed wave transmission, whereby wave

propagation in one direction is initially impeded and resumes only after a duration delay. Based

on numerical evidence, we construct a nonlinear reduced-order model (ROM) to further study

this phenomenon, and show that it is caused by energy accumulation, instability and a transition

between distinct branches of certain nonlinear normal modes (NNMs) of the ROM. The

implications and possible practical applications of our findings are discussed.

* Corresponding author michael.leamy@me.gatech.edu

1

Keywords: Non-reciprocity; nonlinear band structure; amplitude-dependent dispersion;								
metamateria	1							

1 Introduction

In linear time-invariant systems, reciprocity describes the symmetry of wave transmission between a source and a receiver, which can be explained by the Onsager-Casimir principle of microscopic reversibility [1-4]. Breaking reciprocity, or non-reciprocity, has gained significant attention due to its many potential applications, such as wave transmission manipulation [5-7], energy localization and confinement [8, 9], and topological protection [10] in electric circuits, optics [11-13] and acoustics [14-17]. Depending upon the applied field and purpose, various approaches have been investigated to break reciprocity. In electric circuits, non-reciprocity can be directly obtained by electrical elements such as nonlinear semiconductors, diodes, and transistors. In optics, reciprocity has been broken by introducing biased magnetic fields [18], nonlinearity [19], or topological insulating designs [10, 12, 20]. For acoustic and elastic waves, non-reciprocity has been achieved by employing one or a few of the following elements: i) external biases (e.g., unidirectional angular momentum, fluid circulation, or gravity) [21-24], ii) spatio-temporal-modulation [17, 25-29], and iii) nonlinearity [14-16, 30-36]. While considerable research attention has been devoted to the former two active approaches, they require either an external unidirectional field, gain/loss control or parametric modulation, and are therefore energy-consuming and potentially unstable.

Nonlinearity on the other hand, when combined with structural/geometric asymmetry, has the ability to break reciprocity in a purely passive way. Liang *et al.* realized an acoustic rectifier by altering the sending frequency using a nonlinear medium and then filtering the resulting signal through a superlattice [15, 16]. Shortly after, Boechler *et al.* utilized an asymmetrical bifurcation in a granular crystal and built a tunable acoustic rectifier [33]. Recently, the authors in [14, 30,

31] theoretically and experimentally studied non-reciprocal wave transmission in an asymmetrical, hierarchically structured waveguide employing cubic stiffness springs. Later, Wu et al. developed a metastable structure where the range of non-reciprocity can be predicted via the harmonic balance method [32, 34]. Due to the nonlinearity converting significant energy to other harmonics, the non-reciprocity achieved in these previous studies is limited by distortion of the sending frequency or restricted operation range. Hence, most recently, by locally implementing mass asymmetry and cubic coupling in a one-dimensional waveguide, Darabi et al. experimentally developed a passive device, consisting of a single unit cell, that preserves the signal frequency while obtaining directional energy transmission over a broad operation range [37].

In this paper, we propose a 1D *metamaterial* (in contrast to the *device* realized in [37]) which breaks reciprocity over a broad range of frequencies with minimal signal distortion and high energy transmission in a single (preferential) direction. The metamaterial employs strongly nonlinear springs and a triangle-shaped topological asymmetry, inspired by the quantum non-reciprocity studied by Li *et al.* [38]. The band structure of this system is computed numerically adopting a wavenumber-frequency-amplitude representation, through which directional dispersion and tunable non-reciprocity is observed. In addition to the conventional non-reciprocity, we observe, document, and investigate the new nonlinear phenomenon of time-delayed wave propagation; that is, a signal propagates through the metamaterial in one direction; but in the other direction it is impeded for a period of time and then resumes propagation. A nonlinear reduced-order model (ROM) is constructed to study and understand this phenomenon.

2 System description

Figure 1a depicts a schematic representing the proposed metamaterial: a shear lattice containing a chain of repetitive nonlinear triangle-shaped unit cells. Each nonlinear unit cell is composed of 16 particles (blue spheres) connected by linear/nonlinear connectors (green/red rods). Each particle, considered as a point mass, is restricted to only oscillate in the z direction, resulting in transverse wave generation in this metamaterial. As Fig. 1b illustrates, the green connector represents a linear spring (stiffness k_1) in parallel with a viscous damper (damping c), whereas the red connector represents a cubic spring (cubic stiffness k_{NL}) in parallel with a linear spring (stiffness k_2) and a damper. Focusing on the non-reciprocal behavior of this metamaterial, we

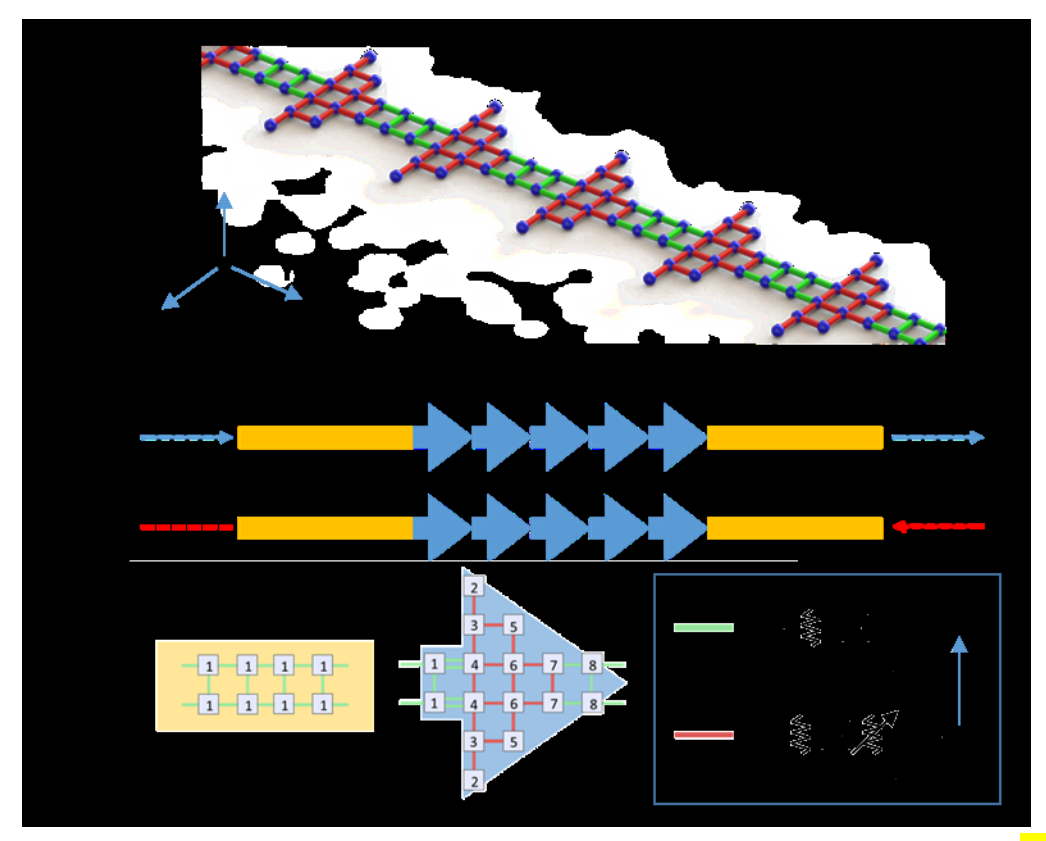


Figure 1 System Description. a) Rendered representation of the metamaterial. b) Detailed discrete structure of the unit cell (blue), waveguide (yellow), and connectors (in the blue frame). The blue arrow in the frame indicates the orientation of the schematic. The signal is generated at either end of the system. Non-reciprocity occurs when the propagation is allowed for left-to-right, but prevented in the opposite direction.

select five unit cells and situate them between two identical linear waveguides (stiffness k_1). The model has a free-free boundary condition. Based on the experimental data provided in [37], we select and present the system parameters in Table 1 below.

Table 1 System parameters of the depicted system.

Parameter	$m_1, m_5, m_6 \& m_8$	m_2	m_3	m_4	m_7
Value	0.05 kg	0.0616 kg	0.0733 kg	0.7 kg	0.3911 kg
Parameter	k_1	k_2	k_{NL}		
Value	200 N/m	20 N/m	2E9 N/m^3		

While the masses in each nonlinear unit cell are not identical, they maintain a top-bottom symmetry, and hence, the wave propagation through the metamaterial is essentially one-dimensional. Note that, in the following study, we consider an undamped system (c=0). The effect of damping will be discussed in section 5. The governing equation of motion is expressed as

$$m^* \ddot{x^*} + k_1 \sum_i (x^* - x_i) + k_2 \sum_j (x^* - x_j) + k_{NL} \sum_j (x^* - x_j)^3 + c \sum_p (\dot{x^*} - \dot{x}_p) = 0$$
 (1)

where m^* and x^* denotes the mass and displacement of the particle of interest; subscripts i and j refer to the neighboring masses connected by linear and nonlinear coupling, respectively; and subscript p refers to all the masses surrounding the studied mass. The dynamic behavior of the system is thus obtained by performing direct numerical integration of Eq. (1).

To excite the system, we send continuous harmonic waves at a constant magnitude and frequency, modified by a Hann window by prescribing the displacement of the mass at the end of one linear waveguide (sending waveguide), and measure the response accordingly at the other waveguide (receiving waveguide). In that way we can study left-to-right (L-R) or right-to-left (R-

L) wave transmission through the nonlinear array. In fact we will be interested only in primary wave transmission, that is on the nonlinear scattering of the impeding wave packet from either side and we won't be concerned by secondary waves that result from reflections of waves at the free boundaries of the left and right waveguides (i.e., the sender and receiver waveguides). Accordingly, the waveguides are designed to be sufficiently long such that any possible reflections from the nonlinear unit cells do not interfere with the source. Therefore, importantly, we ensure the same input energy for both propagation directions so that we can study the nonlinear acoustic non-reciprocity of this metamaterial at a prescribed energy level.

3 Wavenumber-frequency-amplitude band structure

The proposed metamaterial exhibits spatial periodicity, which naturally leads to a band structure. At low input amplitude, the linear term in the nonlinear coupling dominates the restoring force, and thus the nonlinear term can be omitted. Therefore, the dispersion relationship of the linearized system is obtained by solving the eigenvalue problem described below [39],

$$[K(\mu) - \omega^2 M]\tilde{\mathbf{u}}(\mu)e^{in\mu} = 0 \tag{2}$$

where μ denotes the propagation constant (wavenumber in discrete system), ω the angular frequency, and M, K the mass and stiffness matrices, respectively. The resultant dispersion relationship is presented in Fig. 2 where the frequency range of interest is highlighted in Fig. 2a

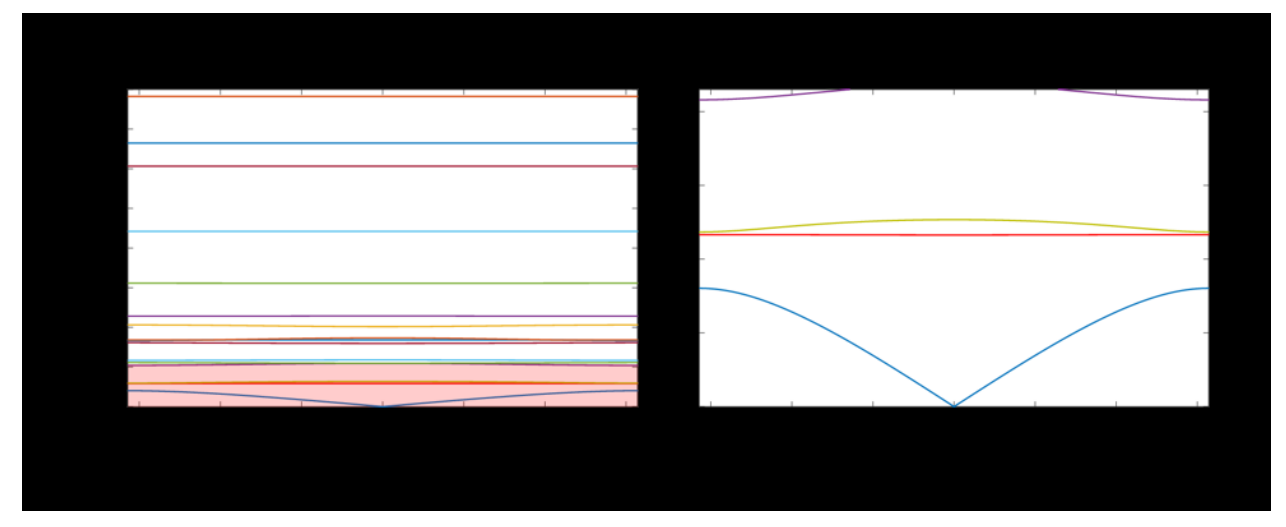


Figure 2 Linear Dispersion Relationship. a) This graph shows the solution of the eigenvalue problem in Eq.2. The frequency range of interest is highlighted in the red block. **b)** Close inspection of dispersion relationship detailing the acoustic and three optical branches.

and a detailed view is shown in Fig. 2b. The procedure for obtaining dispersion curves is documented in Appendix I.

Though the band structure for low input can be approached via system linearization, it is challenging to solve for the dispersion relationship at higher amplitudes where nonlinear terms not only cannot be neglected, but, rather become dominant. Here, we introduce a new representation under which we are able to numerically determine the amplitude dependency of nonlinear dispersion. Accordingly, we i) sweep the input wave's frequency and amplitude to obtain the associated responses, then ii) measure the corresponding propagation constants in the nonlinear domain using a relative phase method [40], and finally iii) display the band structure using a wavenumber-frequency-amplitude diagram. Below, we provide details of the relative phase method.

As described in Fig. 3, we capture the time responses of two masses at the same corresponding locations of two adjacent unit cells (Fig. 3a-b) and compute the phase of each dominant

frequency harmonic component (Fig. 3c-d). Then, assuming that stationary (steady state) wave transmission has been reached, the difference between the phases approximately reveals the real part of the propagation constant. Finally, according to the zone folding principle, we fold the resultant propagation constant into the First Brillion Zone ($\mu \in [0,\pi]$). The operations are presented below,

$$G_n(\omega) = fft(x_n(t_1:t_2)) \tag{3}$$

$$a_n(\omega^*) = Re(G_n(\omega^*)) \tag{4}$$

$$b_n(\omega^*) = Im(G_n(\omega^*)) \tag{5}$$

$$\theta_n(\omega^*) = \tan^{-1}\left(\frac{b_n(\omega^*)}{a_n(\omega^*)}\right) \tag{6}$$

$$Re(\mu) = \theta_n(\omega^*) - \theta_{n+1}(\omega^*), \tag{7}$$

where x_n denotes the time response of the selected mass in the n^{th} nonlinear unit cell, with t_1 and t_2 marking the start and end time of the sampled signal. While t_2 is selected at the end time of the simulation, t_1 is selected to be away from the time when the signal reaches the receiving waveguide to avoid possible transient behavior. The duration (t_2-t_1) is equal to an integer number of sending signal periods. The dominant frequency ω^* is obtained using a Fast Fourier Transformation (FFT), and its amplitude $G_n(\omega^*)$ is accordingly decomposed into real and imaginary parts, namely $a_n(\omega^*)$ and $b_n(\omega^*)$, to obtain the phase $\theta_n(\omega^*)$. The phase difference from one nonlinear unit cell to the next determines the real part of the propagation constant.

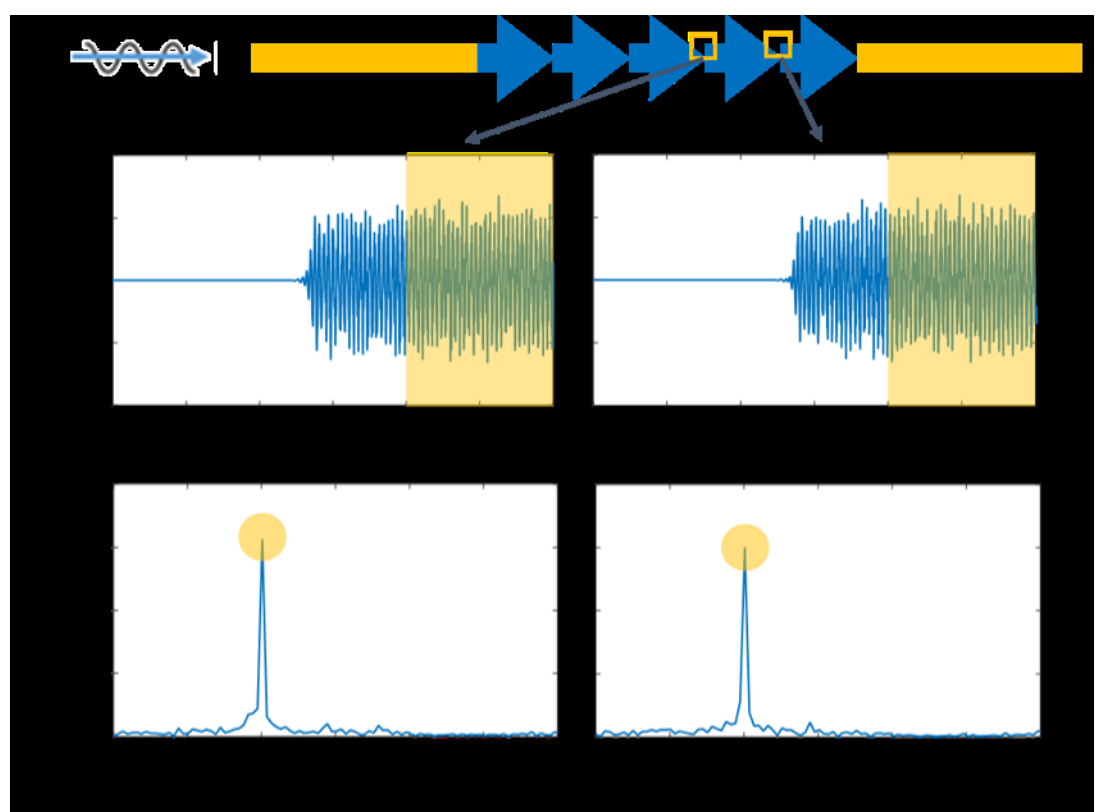


Figure 3 Propagation Constant Measurement. a) Time response of the first mass of the fourth unit cell when the wave propagates from left to right. b) Time response of the first mass of the fifth unit cell. c) Frequency response of the yellow highlighted region in Fig. 3a. d) Frequency response of the yellow highlighted region in Fig. 3b.

The proposed method is preferred over a spatial FFT of a snapshot of the response, since the resolution of the spatial FFT method depends upon the number of sampling points, which in this case is no more than the finite number of unit cells in the nonlinear unit cell domain. However, it is challenging for both methods to numerically measure the wavenumber near π , where the group velocity approaches zero. Therefore, a modified polynomial curve fitting is employed to locate the bandgap and extrapolate the dispersion curves near these points. The details of the curve fitting process are documented in Appendix II.

4 Non-reciprocity Measure

The resulting nonlinear band structure for the system defined in Table 1 is provided in Fig. 4a. We only depict the acoustic branch and the first optical branch for ease of presentation, and ensure that the other branches are far from the concerned range of frequency or sufficiently flat (narrow passband and near-zero group velocity whose influence on wave propagation is negligible). Close inspection of Fig. 4a reveals that i) as the input amplitude increases, the dispersion curves shift upwards, which indicates nonlinear hardening behavior due to the positive cubic stiffness nonlinearities of the unit cells; ii) at each amplitude, the blue (left-to-right) dispersion curve differs from the red (right-to-left) one, which results in non-reciprocal energy transmission. Note that the small fluctuations in the dispersion curves are caused by noise in the numerical data so they represent numerical artifacts with no physical meaning.

Figure 4b provides a detailed view of the low-frequency band structure at a single amplitude (highlighted in green in Fig. 4a). Additionally, Figure 4b provides a measure of non-reciprocity, δ , depicted by horizontal bars at each selected frequency (corresponding to the top axis). Inspired by the non-reciprocity measure proposed by Blanchard *et al.* [41], we define our measure as,

$$\delta = \frac{\int_{t_1}^{t_2} |E_{LR} - E_{RL}| dt}{\int_{t_1}^{t_2} |E_{LR} + E_{RL}| dt} , \qquad (8)$$

where t_1 and t_2 denote the start and end of the selected time duration (same duration in Eq. 4), and E_{LR} and E_{RL} the transmitted energy contained in the farthest nonlinear unit cell from the signal source for L-R and R-L propagation, respectively. As indicated in Eq. 8, this measure compares the difference between the transmitted energy of two responses. The chosen non-reciprocity measure is bounded between 0 and 1, where $\delta \to 0$ indicates complete reciprocity,

and $\delta \to 1$ indicates "giant" non-reciprocity (i.e., complete absence of transmission in one of the two directions of wave propagation). The color of these horizontal bars indicates the energy level

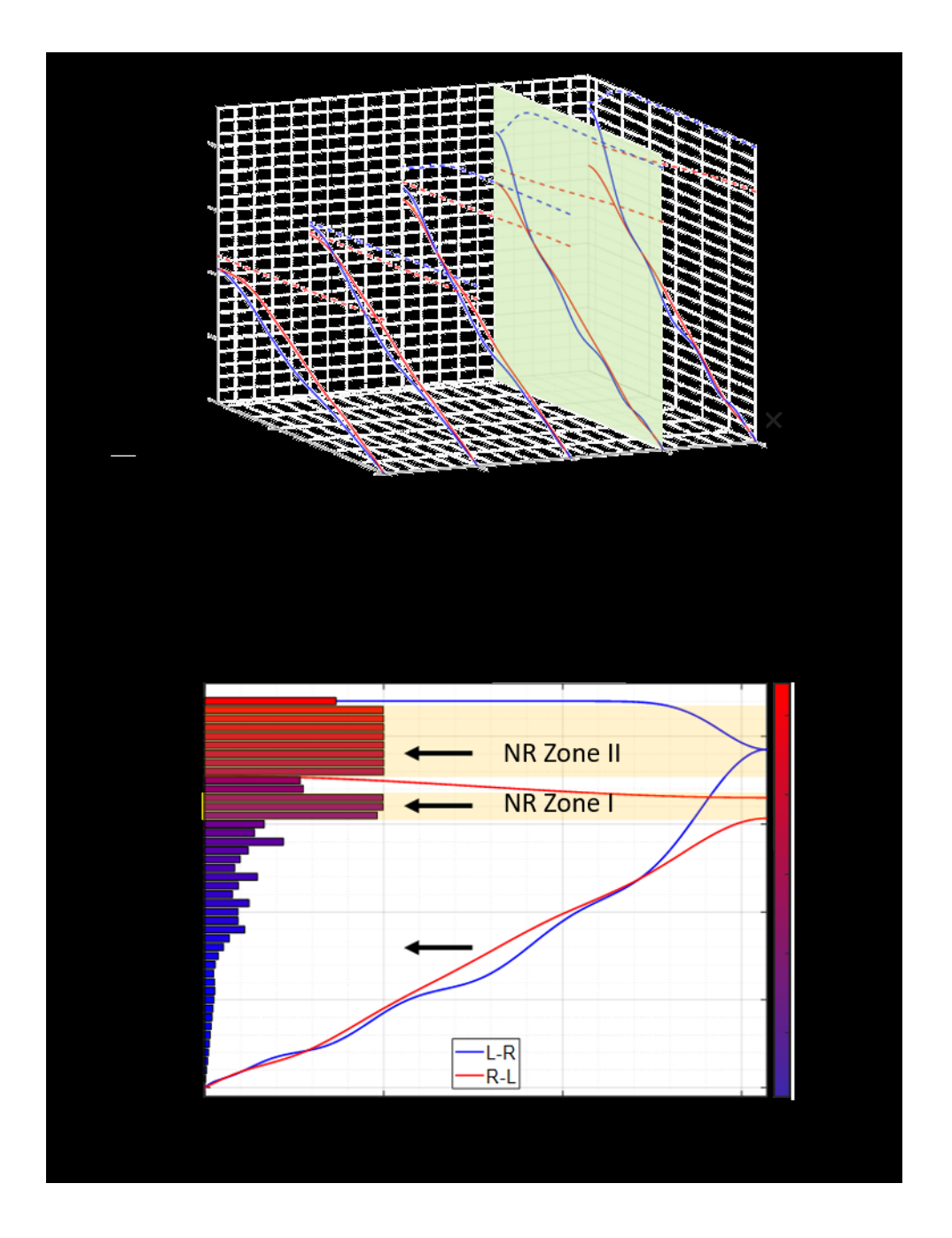


Figure 4 Non-reciprocity Analysis a) Wavenumber-frequency-amplitude band structure, where acoustic (solid lines) and one optical (dashed lines) branches are depicted. **b)** Dispersion relationship at input amplitude = 0.2mm, with the non-reciprocity measure shown as horizontal bars. The color bar represents the energy level at the source.

of each individual signal. Since the signal amplitude is fixed, a higher frequency signal contains higher energy.

From the non-reciprocity measure, we observe reciprocal energy transmission at low frequency and giant non-reciprocity at highlighted regions (labeled NR Zones I and II). This result provides a good match to the nonlinear band structure: i) The low-frequency signal falls in the passband of both directions; ii) the non-reciprocity regions fall in the passband of the L-R direction, but, at the same time in the stopband of R-L direction; iii) the two non-reciprocity regions are separated by the optical branch for the R-L direction, in which the R-L propagation resumes and the non-reciprocity measure drops significantly.

Furthermore, we study in detail the transmitted signals in the reciprocal region and both non-reciprocal zones. We select and depict time/frequency responses of the first mass in the receiving waveguides, at three input frequencies, each of which derives from one characteristic region (indicated by black arrows in Fig. 4b). The time responses are presented on the left of Fig. 5 and the corresponding frequency responses are plotted on the right of the time responses. Note that, the amplitudes in the frequency domain are normalized with respect to the source amplitude. In Fig. 5a-b, low-frequency input results in reciprocity, while in Figs. 5c &e, there is a high transmission ratio for L-R propagation (blue curves) in both non-reciprocity zones, and relatively low transmission ratio in the other direction. The transmission loss can be attributed to two major factors: i) the reflection at the interface between the linear waveguide and the nonlinear unit cells; and ii) the energy exchanges between the source frequency and the generated harmonics. In the frequency domain, Figs. 5d &f reveal that, despite other harmonics generated by the

nonlinearity, the sending frequency of the L-R signal remains dominant, whereas the R-L receiving spectrum approaches a low-level noise.

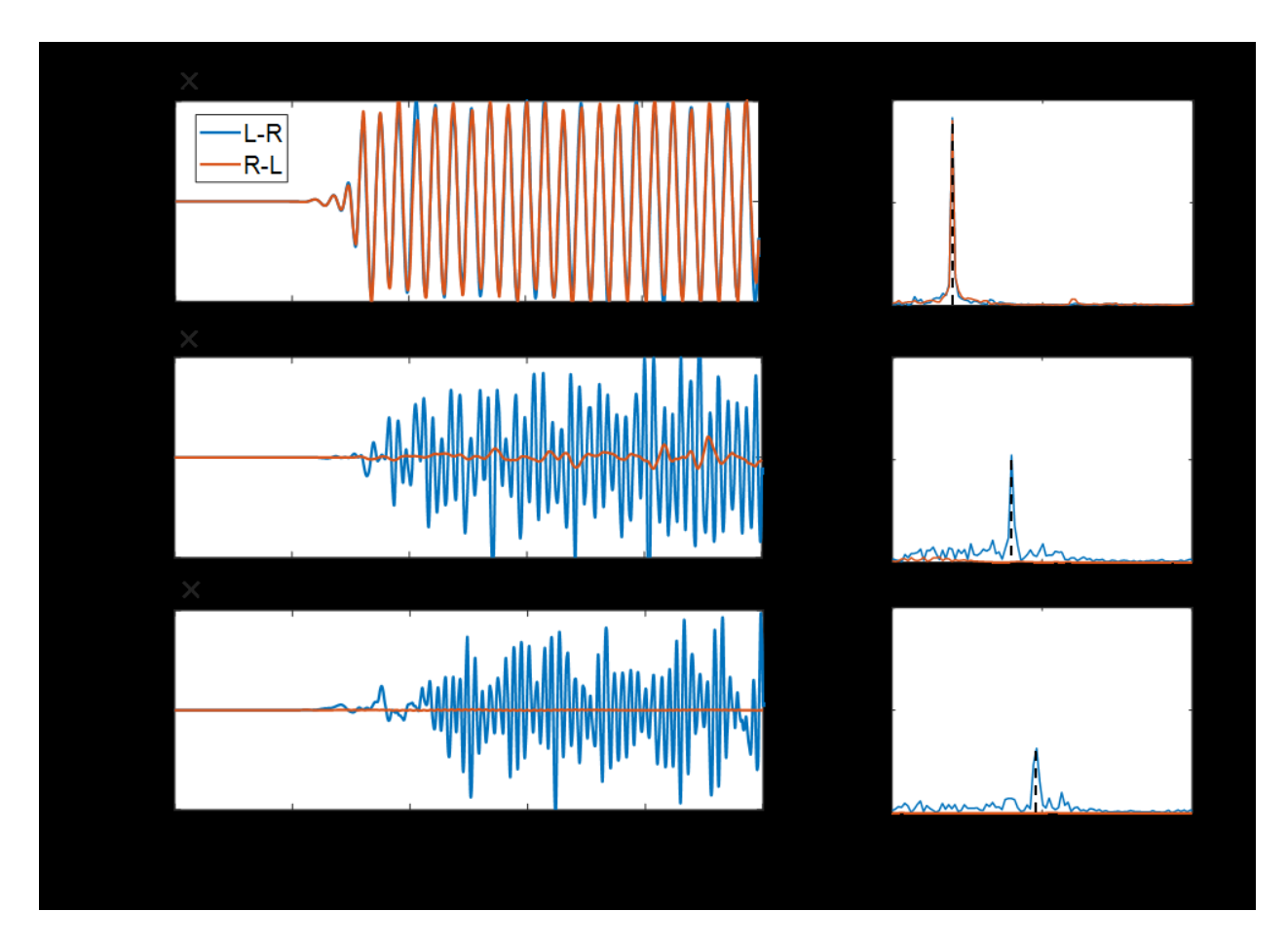


Figure 5 Time and frequency responses of transmitted wave. Responses of three sending signals (8 rad/s, 16 rad/s, and 19 rad/s) are presented. Each FFT plot refers to its left time response, and the vertical axis in each FFT plot refers to the ratio of response amplitude to source amplitude. Blue and red curves represent L-R and R-L propagation, respectively.

5 Time-Delayed Propagation

By further increasing the simulated time extent in the NR zones presented, we observe a new nonlinear behavior in the proposed metamaterial and term it "time-delayed propagation." L-R wave transmission is realized straightforward through the nonlinear unit cells; however, R-L propagating waves are at first arrested, partially reflected back, and then later transmitted

through the nonlinear cells with a certain time delay compared to L-R wave transmission. Fig. 6a describes the phenomenon by comparing the response in the receiving waveguide for L-R and R-L subject to a sending signal at frequency 18 rad/s and amplitude 2×10^{-4} m (within the NR Zone II in Fig. 4b). We observe that the L-R transmission occurs at the $1^{\rm st}$ quarter of the time window, while the R-L propagation is impeded until the last quarter, after which the propagation resumes. Fig. 6b further presents the wavelet results of both signals. It is clear that both signals exhibit a frequency broadening effect, yet only the L-R signal preserves the sending frequency. Note that, in the following study, we prefer the wavelet transformation over an FFT to study the frequency

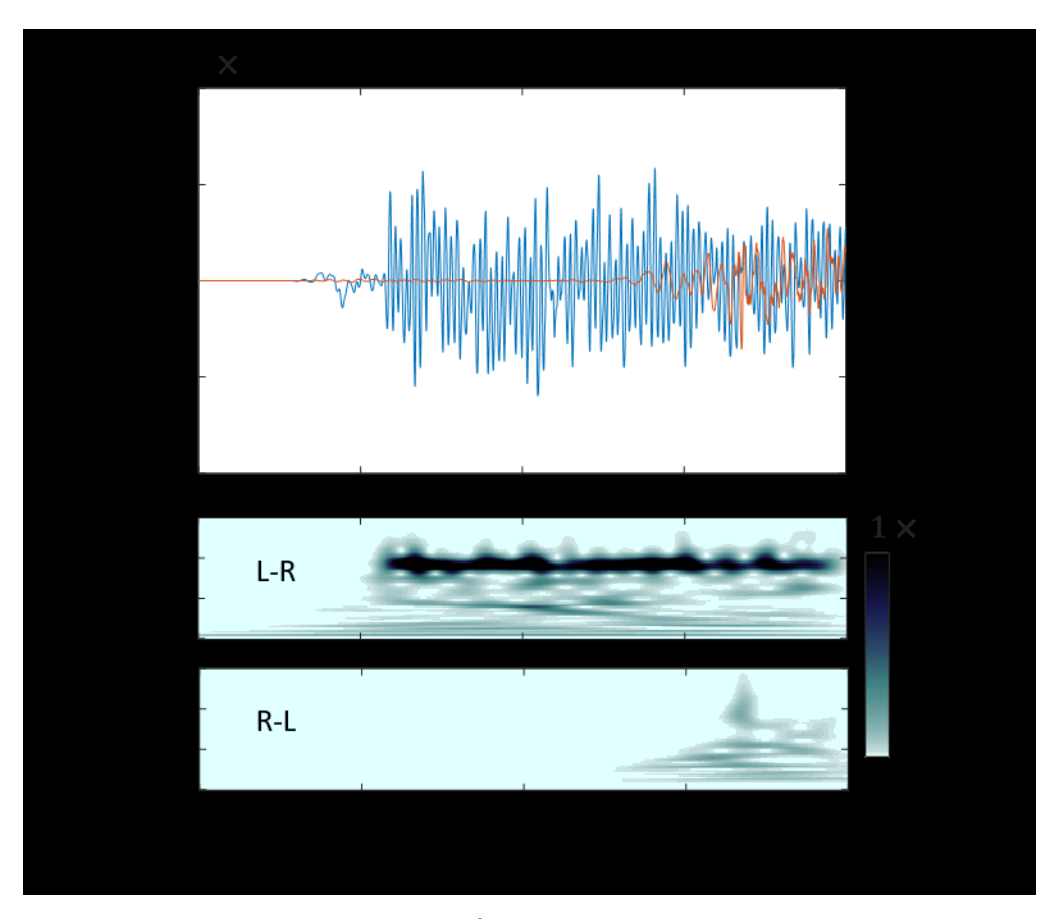


Figure 6 Time-delayed propagation. a) Time response of the receiving signal for both directions at frequency 18 rad/s, amplitude 2×10^{-4} m. Note that, the L-R and R-L signal are denoted blue and red, respectively. b) Wavelet response of the L-R and R-L receiving signal.

content since the wavelet spectra provides additional information about the time-evolution of frequencies in nonlinear systems.

This phenomenon can be qualitatively explained by energy accumulation and stability transition of the excited nonlinear normal modes (NNMs) at the interface between the nonlinear unit cells and the sending waveguide. Consider the same sending signal used in Fig. 6 (frequency 18) rad/s and amplitude 2×10^{-4} m), which lies in the L-R passband but also in the R-L stopband. When the R-L wave reaches the first nonlinear unit cell, a large portion of the wave energy reflects back into the sending waveguide; however, a small portion of energy remains in the nonlinear unit cells. Locally, this process appears as the emergence of an NNM at the interface. As the residual energy fluctuates and slowly accumulates, the response moves along the frequency-energy NNM branch and approaches a bifurcation point where the response jumps from one branch to another (this process is studied further below), which opens the gate for the sending wave and resumes the propagation. The duration of such energy accumulation and stability transition is observed as the "delay" in the time response. At fixed frequency, a larger amplitude has a faster energy accumulation process, resulting in a shorter delay, and vice versa. Additionally, this delay can be elongated by introducing energy dissipation, which we discuss at the end of this section.

For further investigation, we first capture the numerical time responses of the masses of the first unit cell encountering the R-L signal, as shown in Fig. 7a. We observe that before the propagation resumes at the time instant t^* (indicated by the black dashed line in Fig. 7a), masses 6, 7, and 8 have large displacements compared to masses further along the chain (we do not consider mass 2, since it is far from the main transmission line masses 1- 4- 6- 7- 8). Accordingly, we establish a

reduced-order model (ROM) which only contains mass 6, 7 and 8 in order to study the interface dynamics, as presented in Fig. 7b. Noteworthy, due to the negligible displacements of masses 4 and 5, in the ROM they are replaced by two rigid walls grounding mass 6. By construction we anticipate that the ROM will be only valid up until t^* . Beyond this time, propagation commences and the ROM is no longer applicable. Moreover, the ROM is assumed to be excited by the actual motion of mass 8, which is taken to be the displacement computed in the full-order model (highlighted in yellow in Fig. 7c). The ROM is further validated by comparing the responses of masses 6 and 7 to those from the full-order model. The comparison is detailed in Fig. 7c, where we find a good agreement before t^* , as expected. Therefore, we proceed the investigation by performing an NNM and wavelet analysis based on this ROM in order to gain understanding on the nonlinear mechanism that governs the previous non-reciprocal time delay in the R-L transmitted waves.

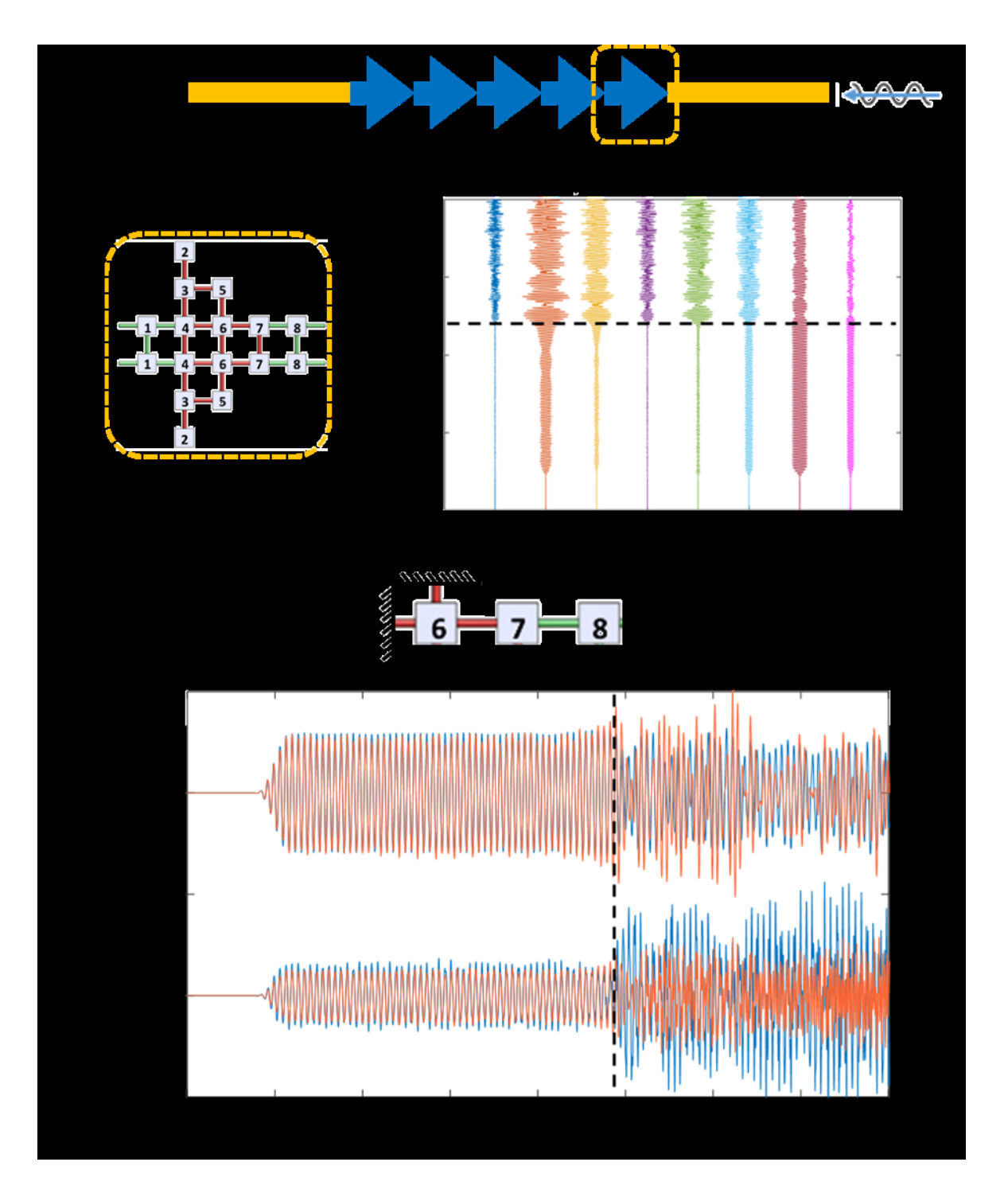


Figure 7 Displacement distribution and reduced-order model. a) Time response distribution of the first unit cell encountering the R-L signal. Displacements of masses 1, 3, 4, and 5 are negligible compared to those of masses 6, 7, 8 before the highlighted time t^* , indicated by the dashed black line. b) Schematic of the reduced-order model c) Time responses of masses 6, 7 from the full-order model (blue) and the reduced-order model (red). Similarly, the black dashed line indicates the moment of destabilization. Note that, in the reduced-order model the motion of mass 8 is prescribed to be the same as mass 8 in the full-order model.

An NNM is a two-dimensional invariant manifold in phase space, which describes a distinct periodic solution near each stable equilibrium at fixed energy levels of a Hamiltonian system [9, 42]. As detailed in [42-44], an NNM analysis of a discrete or continuous dynamical system sweeps the energy in the system and solves for the modal frequency and associated mode shape, which provides important information on frequency-shifting, energy-dependent response, stability, and bifurcation structure of the dynamics. With regard to the previously derived ROM, this

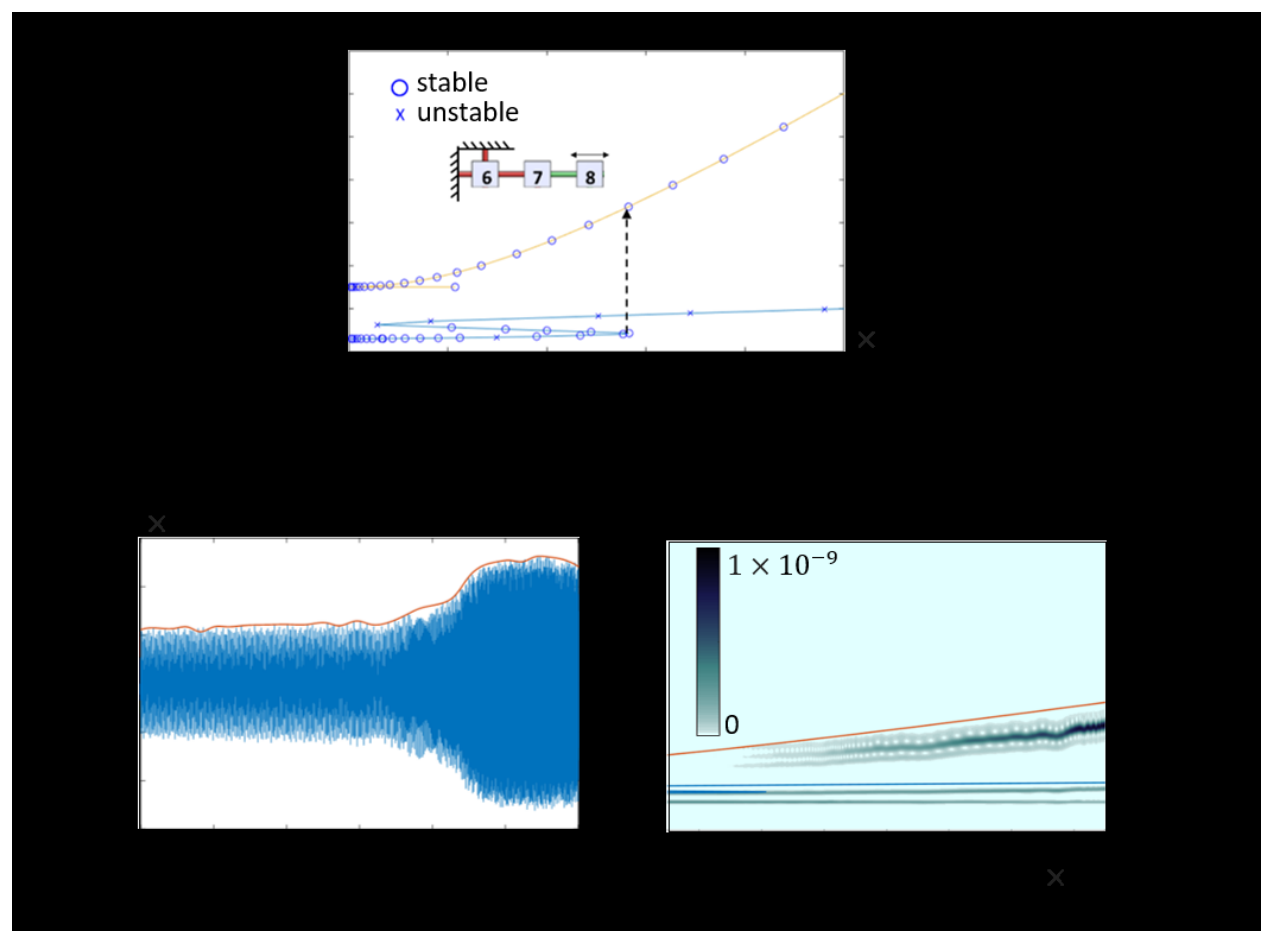


Figure 8 Nonlinear normal mode and wavelet response of the reduced-order model. a) The NNM computation result. The horizontal axis depicts the relative displacement between masses 6 and 7. The vertical axis depicts the associated mode frequency. The two branches are distinguished by color. Circular markers denotes stable modes, and cross markers denotes unstable modes. b) Relative displacement between masses 6 and 7 when subject to harmonic motion of mass 8. The red line marks the wave envelope. c) The superposition of the NNMs and the wavelet result from the reduced-order model. Note that the wavelet result has been adapted to a relative displacement axis based on the envelope in Fig. 8b.

system exhibits two degrees of freedom (since the motion of mass 8 is prescribed), and results in two families of NNMs (note that the number of NNMs of a discrete system may exceed its degrees of freedom due to mode bifurcations – this is exactly the case herein). With details of the NNM computation provided in Appendix III, we present the NNM results for the ROM in Fig. 8a above.

As depicted, the NNM result reveals the relationship between modal frequencies and relative displacement between masses 6 and 7, with round/cross markers illustrating stable/unstable modes, respectively. According to the NNM results, a bifurcation occurs at a relative displacement near $1.4 \times 10^{-4} \, m$. Beyond this point, the first mode loses stability, and the response jumps to the second branch (as indicated by the dashed arrow in the figure).

To verify this bifurcation behavior in the reduced-order model, we prescribe harmonic excitation to mass 8 and compare the response to the obtained NNMs. As such, we capture the time response of the relative displacement between masses 6 and 7 in Fig. 8b, and use an envelope function to obtain its response amplitudes. Then, we conduct the wavelet transformation on the response and convert its time axis to relative displacement amplitude according to the envelope. Finally, in Fig. 8c, we superimpose the topology of the NNMs on the converted wavelet response. We observe three major frequency branches. The lowest branch represents the sending frequency (18 rad/s); the middle branch matches the first mode (23 rad/s) in the NNM result; and the highest branch represents the second mode emerging at approximately 0.7A, which agrees well with the NNM prediction. Note that the first mode is present even after the bifurcation point, because this ROM is subject to continuous input, which saturates the energy of this mode. The second mode is slightly lower in frequency than the NNM prediction, as

expected, since the NNM computation does not consider the energy distribution between modal frequencies.

We then compare the NNMs with the wavelet response of our full-order model. Similarly, we obtain the envelope from the time response of the relative displacement between masses 6 and 7 (Fig. 9a), and superimpose the NNMs result onto the wavelet result in Fig. 9b. We observe that before the bifurcation point at a relative displacement of $1.4 \times 10^{-4}~m$, the sending frequency dominates the motion. As the amplitude of relative displacement increases and surpasses the bifurcation point, multiple frequencies appear, which cannot be described by the NNM result of the ROM as expected. This observation indicates that the stability-transition at the bifurcation point affects the motion of masses 4 and 5, which can no longer be considered as walls, and therefore results in the inapplicability of the ROM and the resumption of wave transmission through the nonlinear cell from this point on.

In summary, the NNM and wavelet analysis reveals: i) for R-L wave transmission, a stable NNM is formed at the first unit cell encountering the wave, which prevents the wave from propagating as the energy of the impeding wave from the right linear waveguide accumulates at the interface as it excites that NNM; ii) the formed NNM loses stability above a certain threshold of energy accumulation, in particular, when the relative displacement between mass 6 and 7 grows larger than $1.4\times 10^{-4}~m$, and the wave resumes propagating through the nonlinear cell with broadened frequency content.

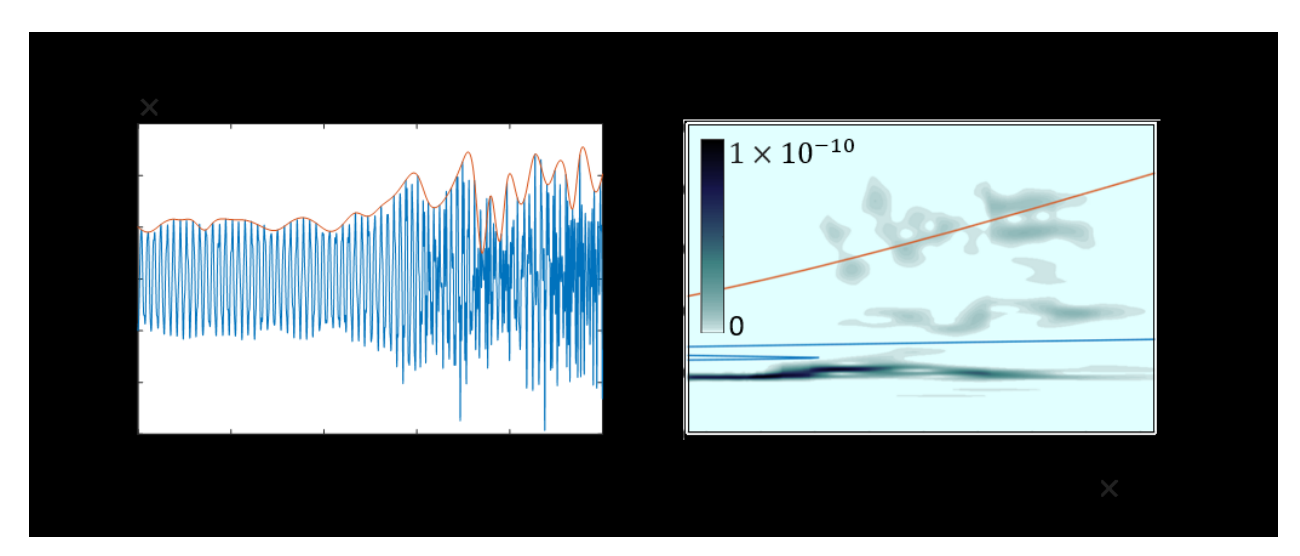


Figure 9 The nonlinear normal mode and wavelet result for the full-order model. a) Relative displacement between masses 6 and 7 at the interface of the first unit cell encountering the R-L propagating signal. The red line marks the wave envelope. b) Superposition of the nonlinear normal modes of the ROM and the wavelet result from the full-order model simulation. Note that, the wavelet result has been adapted to a relative displacement axis based on the envelope in Fig. 9a.

Additionally, we observe that the duration of the time-delay is highly sensitive to energy dissipation in the cells. In Fig. 10a, we introduce a light viscous damping ($c = 2 \times 10^{-4} \text{ kg/s}$) in the nonlinear unit cells, and compare the receiving response with that of an undamped model (Fig. 10b) subject to the same input signal (frequency 18 rad/s and amplitude 2×10^{-4} m). Clearly, the time-delayed propagation now occurs later. Practically, a large-enough damping can even eliminate the time-delayed propagation and achieve strict non-reciprocity by dissipating the accumulated energy and thus avoiding the bifurcation.

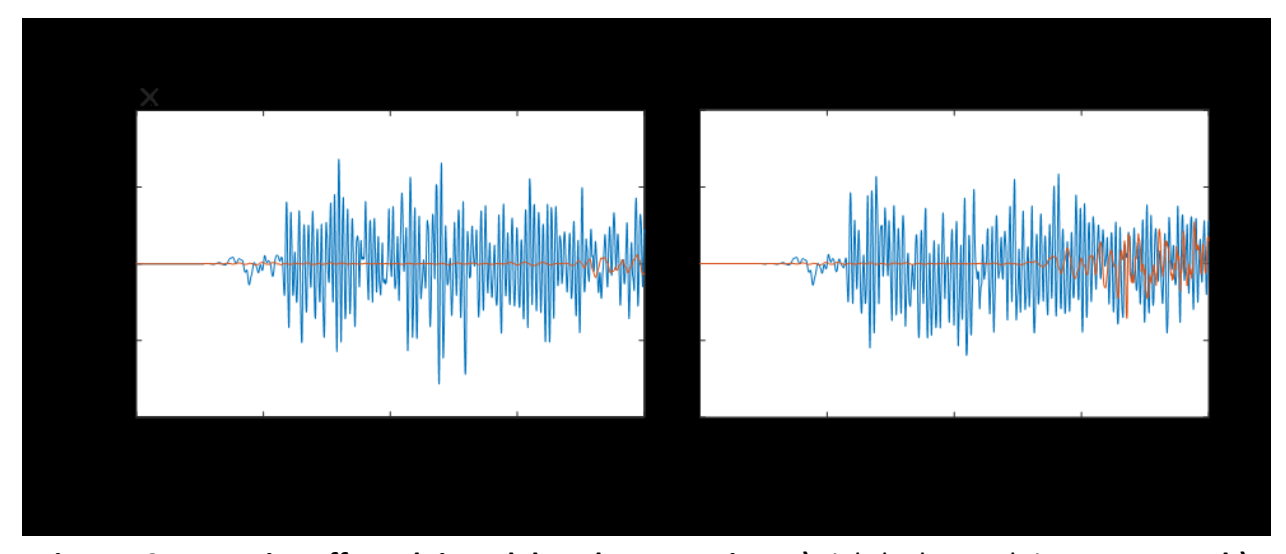


Figure 10 Damping affected time-delayed propagation. a) Lightly damped time response. b) Undamped time response for the same input. L-R and R-L signal is denoted by blue and red, respectively.

6 Concluding Remarks

In this paper, we perform a numerical study of a strongly nonlinear one-dimensional metamaterial and demonstrate its non-reciprocal behavior subject to harmonic excitation at either one of its ends. Compared to previous studies, the achieved non-reciprocity exhibits several desired properties: i) broadband operation range, ii) robust signal integrity, and iii) high transmission ratio. Using a wavenumber-frequency-amplitude band structure construct, we match the observed reciprocal/non-reciprocal behavior to amplitude-dependent dispersion characteristics. Furthermore, we observe, document, and numerically investigate a new nonlinear phenomenon, namely, time-delayed wave transmission in one of the two possible directions of propagation. Using a reduced order model we demonstrate that this phenomenon can be qualitatively explained by energy accumulation and stability transition of nonlinear normal modes at the interface between the first nonlinear cell encountered and the linear waveguide

where initially the wave propagates. Finally, we find the delay duration can be increased by the presence of damping, so it has tunable characteristics.

Conflict of Interest

The authors declare that they have no conflict of interest.

Acknowledgement

The authors would like to thank the National Science Foundation for supporting in part this research under the Emerging Frontiers in Research and Innovation (EFRI) Grant No. 1741565.

Appendix

I. Linear Dispersion Analysis

The dispersion relationship of a linear periodic structure can be pursued by solving the eigenvalue problem of the equations of motion with Bloch boundary conditions [39]. Here, we reconsider Eq. 2 below with a detailed study,

$$[K(\mu) - \omega^2 M]\tilde{\mathbf{u}}(\mu)e^{in\mu} = 0, \tag{A. 1}$$

where M and $K(\mu)$ are mass and stiffness matrix, respectively, and μ denotes the wavenumber. Without loss of generality, we express the non-trivial displacement vector as $\tilde{\mathbf{u}}(\mu)e^{in\mu}$, where n denotes the unit cell of interest. The mass matrix

contains diagonal entries corresponding to the individual masses, and the stiffness matrix $K(\mu)$ is computed from,

$$K(\mu) = \sum_{m=-1,0,+1} (e^{im\mu} k_m),$$
 (A. 2)

where m=-1,0,+1 represents three adjacent unit cells: n-1,n, and n+1, and k_m denotes the conventional stiffness matrix describing the spring interaction within the representative unit cell and with its neighbors. The term $e^{im\mu}$ further modifies the stiffness matrix with Bloch boundary conditions. Thus, by sweeping the wavenumber from 0 to π and solving the eigenvalue problem in term of ω^2 , we obtain the linear dispersion relationship in the First Brillion Zone.

II. Dispersion Curve fitting

In numerical simulations, for each input amplitude, we sweep the frequency of the harmonic input from 0 to 22 rad/s, with an increment of 0.1 rad/s. Propagation constants are then measured from each corresponding response. The scatter points are displayed on the frequency-wavenumber plane, and a curve-fit is conducted as follows:

a. The noise points are recognized based on their dominant frequency (i.e. if the dominant frequency over the selected duration of response is not the sending frequency, the transmitted signal is considered as noise).

- **b.** Branches (in our case only the acoustic and the first optical branches) are recognized manually. Different dispersion curves are curve-fitted individually.
- **c.** A 9-degree polynomial curve fit ("poly9" in MATLAB) is selected as the main fit function.
- **d.** For the acoustic branch, to ensure a zero-group-velocity condition at $\mu=\pi$, we let $x=\sin{(\frac{\mu}{2})}$, and $y=\omega$, and we then find the curve-fit coefficients.
- **e.** For the first optical branch, to ensure zero-group velocity condition at $\mu=0,\pi$, we let $x=\cos{(\mu)}$, and $y=\omega$, and then find the curve-fit coefficients.

An example scatter-point diagram with the corresponding curve-fit result is shown below.

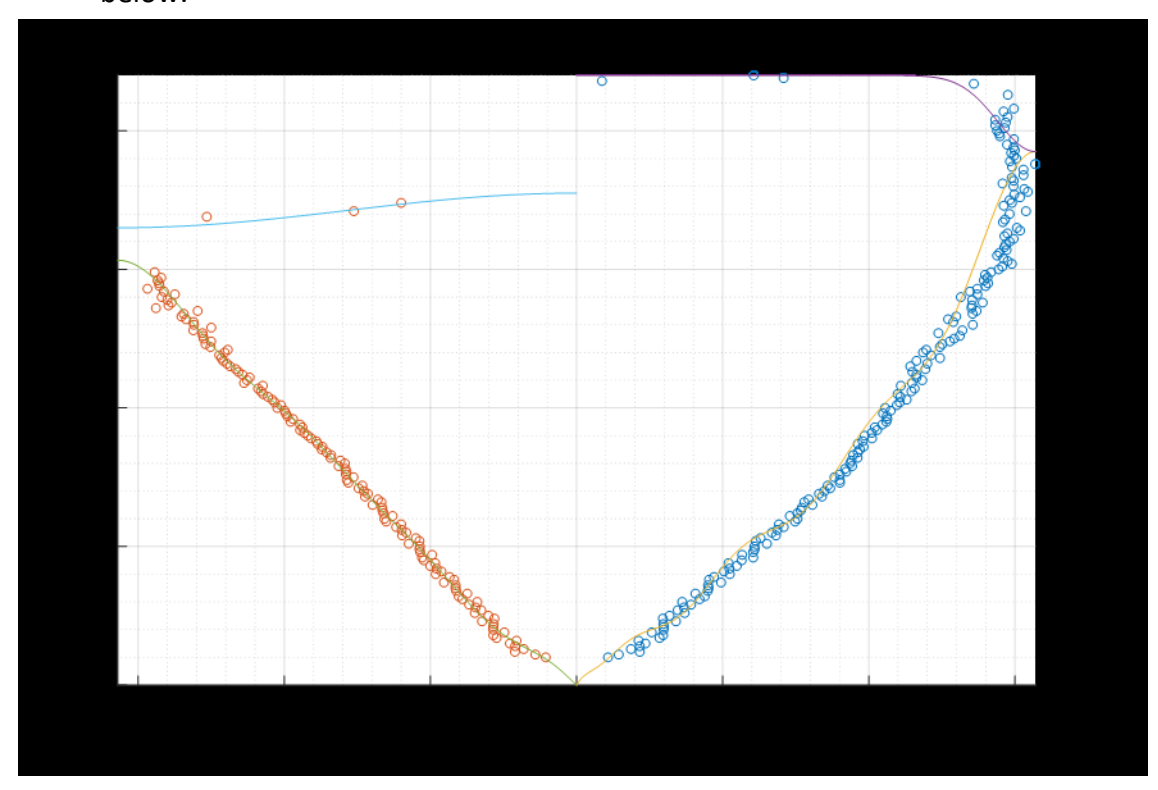


Figure A.1 Scatter points and curve-fit. L-R and R-L propagation constants are marked in blue and red respectively. Four branches (acoustic and optical branches for L-R and R-L wave transmission) are curve-fitted and plotted individually.

III. Nonlinear Normal Modes

For an n degree of freedom Hamiltonian system, there are two fundamental theorems by Liapounov and Weinstein, which indicate n distinct periodic solution(s) near each stable equilibrium at fixed energy level. These solutions are called nonlinear normal modes (NNMs) and can be related to the classic linear vibration modes [36]. By sweeping the energy and solving the equations of motion (see below), we are able to describe the mode frequency and the corresponding mode shape as a function of energy. The resultant NNMs result is revealed in Fig. A.2.

$$m_6\ddot{x}_6 + k_2(3x_6 - x_7) + k_{NL}(x_6 - x_7)^3 + 2k_{NL}x_6^3 + c(3\dot{x}_6 - \dot{x}_7) = 0$$
 (A. 3)

$$m_7\ddot{x}_7 + k_1 x_7 + k_{NL}(x_7 - x_6)^3 + k_2 (x_7 - x_6) + c(2\dot{x}_7 - \dot{x}_6) = 0.$$
 (A. 4)

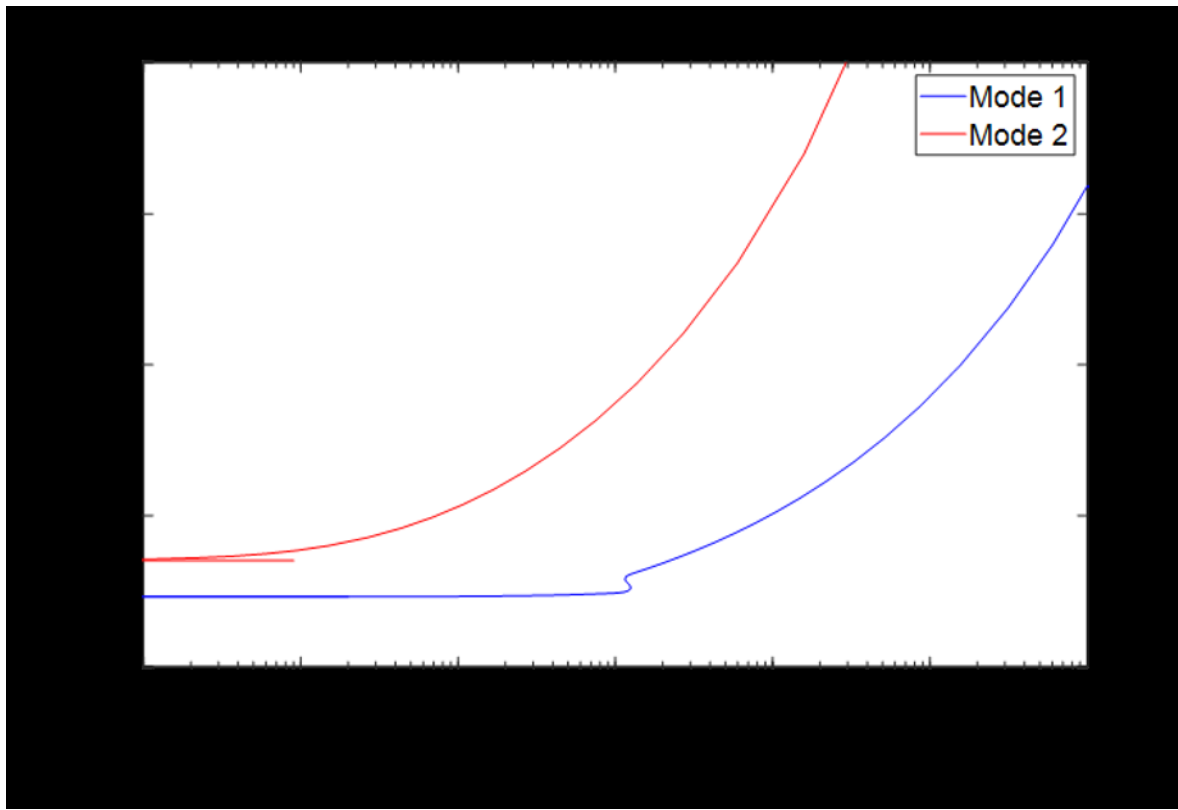


Figure A.2 NNMs result. The NNM frequency-energy relationship.

In the low energy regime (near 10^{-8} J), the frequencies of the nonlinear modes are 23.06 rad/s and 35.08 rad/s, respectively, which is close to the linear natural frequencies of the model. As energy grows, the frequency increases, and Mode 1 experiences a bifurcation at the energy level of approximately 10^{-5} J.

For further investigation and easier comparison with the full-order model, we replace the horizontal axis of the NNM result from energy to relative displacement between mass 6 and 7, illustrated in Fig. 8a. The modification is motivated by the continuous excitation of the system, which makes it challenging to capture the fluctuating energy and conduct further comparison.

References

- [1] Helmholtz, H. v., 1860, "Theorie der Luftschwingungen in Röhren mit offenen Enden," Journal für die reine und angewandte Mathematik, 57, pp. 1-72.
- [2] Strutt, J., 1871, "Some general theorems relating to vibrations," Proceedings of the London Mathematical Society, 1(1), pp. 357-368.
- [3] Casimir, H. B. G., 1945, "On Onsager's principle of microscopic reversibility," Reviews of Modern Physics, 17(2-3), p. 343.
- [4] Onsager, L., 1931, "Reciprocal relations in irreversible processes. I," Physical review, 37(4), p. 405.
- [5] Cummer, S. A., 2014, "Selecting the direction of sound transmission," Science, 343(6170), pp. 495-496.
- [6] Fleury, R., Sounas, D., Haberman, M. R., and Alu, A., 2015, "Nonreciprocal acoustics," Acoustics Today, 11(EPFL-ARTICLE-223074), pp. 14-21.
- [7] Cummer, S. A., Christensen, J., and Alù, A., 2016, "Controlling sound with acoustic metamaterials," Nature Reviews Materials, 1(3), p. 16001.
- [8] Darabi, A., and Leamy, M. J., 2017, "Clearance-type nonlinear energy sinks for enhancing performance in electroacoustic wave energy harvesting," Nonlinear Dynamics, 87(4), pp. 2127-2146.
- [9] Vakakis, A. F., Manevitch, L. I., Mikhlin, Y. V., Pilipchuk, V. N., and Zevin, A. A., 2001, Normal modes and localization in nonlinear systems, Springer.
- [10] Lu, L., Joannopoulos, J. D., and Soljačić, M., 2014, "Topological photonics," Nature Photonics, 8(11), p. 821.
- [11] Khanikaev, A. B., and Shvets, G., 2017, "Two-dimensional topological photonics," Nature Photonics, 11(12), p. 763.
- [12] Rechtsman, M. C., Zeuner, J. M., Plotnik, Y., Lumer, Y., Podolsky, D., Dreisow, F., Nolte, S., Segev, M., and Szameit, A., 2013, "Photonic Floquet topological insulators," Nature, 496(7444), p. 196.

- [13] Mahmoud, A. M., Davoyan, A. R., and Engheta, N., 2015, "All-passive nonreciprocal metastructure," Nature Communications, 6, p. 8359.
- [14] Bunyan, J., Moore, K. J., Mojahed, A., Fronk, M. D., Leamy, M., Tawfick, S., and Vakakis, A. F., 2018, "Acoustic nonreciprocity in a lattice incorporating nonlinearity, asymmetry, and internal scale hierarchy: Experimental study," Physical Review E, 97(5), p. 052211.
- [15] Liang, B., Yuan, B., and Cheng, J.-c., 2009, "Acoustic diode: Rectification of acoustic energy flux in onedimensional systems," Physical review letters, 103(10), p. 104301.
- [16] Liang, B., Guo, X., Tu, J., Zhang, D., and Cheng, J., 2010, "An acoustic rectifier," Nature materials, 9(12), p. 989.
- [17] Nassar, H., Xu, X., Norris, A., and Huang, G., 2017, "Modulated phononic crystals: Non-reciprocal wave propagation and Willis materials," Journal of the Mechanics and Physics of Solids, 101, pp. 10-29.
- [18] Adam, J. D., Davis, L. E., Dionne, G. F., Schloemann, E. F., and Stitzer, S. N., 2002, "Ferrite devices and materials," IEEE Transactions on Microwave Theory and Techniques, 50(3), pp. 721-737.
- [19] Sounas, D. L., Soric, J., and Alu, A., 2018, "Broadband passive isolators based on coupled nonlinear resonances," Nature Electronics, 1(2), p. 113.
- [20] Sounas, D. L., and Alú, A., 2017, "Time-reversal symmetry bounds on the electromagnetic response of asymmetric structures," Physical review letters, 118(15), p. 154302.
- [21] Sounas, D. L., Caloz, C., and Alu, A., 2013, "Giant non-reciprocity at the subwavelength scale using angular momentum-biased metamaterials," Nature communications, 4, p. 2407.
- [22] Fleury, R., Sounas, D., and Alu, A., 2015, "An invisible acoustic sensor based on parity-time symmetry," Nature communications, 6, p. 5905.
- [23] Fleury, R., Sounas, D. L., Sieck, C. F., Haberman, M. R., and Alù, A., 2014, "Sound isolation and giant linear nonreciprocity in a compact acoustic circulator," Science, 343(6170), pp. 516-519.

- [24] Devaux, T., Cebrecos, A., Richoux, O., Pagneux, V., and Tournat, V., 2019, "Acoustic radiation pressure for nonreciprocal transmission and switch effects," Nature Communications, 10(1), p. 3292.
- [25] Estep, N. A., Sounas, D. L., Soric, J., and Alù, A., 2014, "Magnetic-free non-reciprocity and isolation based on parametrically modulated coupled-resonator loops," Nature Physics, 10(12), p. 923.
- [26] Kamal, A., Clarke, J., and Devoret, M., 2011, "Noiseless non-reciprocity in a parametric active device," Nature Physics, 7(4), p. 311.
- [27] Trainiti, G., and Ruzzene, M., 2016, "Non-reciprocal elastic wave propagation in spatiotemporal periodic structures," New Journal of Physics, 18(8), p. 083047.
- [28] Chen, Y., Li, X., Nassar, H., Norris, A. N., Daraio, C., and Huang, G., 2019, "Nonreciprocal Wave Propagation in a Continuum-Based Metamaterial with Space-Time Modulated Resonators," Physical Review Applied, 11(6), p. 064052.
- [29] Li, J., Shen, C., Zhu, X., Xie, Y., and Cummer, S. A., 2019, "Nonreciprocal sound propagation in space-time modulated media," Physical Review B, 99(14), p. 144311.
- [30] Moore, K. J., Bunyan, J., Tawfick, S., Gendelman, O. V., Li, S., Leamy, M., and Vakakis, A. F., 2018, "Nonreciprocity in the dynamics of coupled oscillators with nonlinearity, asymmetry, and scale hierarchy," Physical Review E, 97(1), p. 012219.
- [31] Fronk, M. D., Tawfick, S., Daraio, C., Vakakis, A. F., and Leamy, M. J., "Non-Reciprocity in Structures With Nonlinear Internal Hierarchy and Asymmetry," Proc. ASME 2017 International Design Engineering Technical Conferences and Computers and Information in Engineering Conference, American Society of Mechanical Engineers, pp. V008T012A023-V008T012A023.
- [32] Wu, Z., Zheng, Y., and Wang, K., 2018, "Metastable modular metastructures for on-demand reconfiguration of band structures and nonreciprocal wave propagation," Physical Review E, 97(2), p. 022209.

- [33] Boechler, N., Theocharis, G., and Daraio, C., 2011, "Bifurcation-based acoustic switching and rectification," Nature materials, 10(9), p. 665.
- [34] Wu, Z., and Wang, K.-W., 2017, "On the wave propagation analysis and supratransmission prediction of a metastable modular metastructure for adaptive non-reciprocal energy transmission," arXiv preprint arXiv:1709.03229.
- [35] Gu, Z.-m., Hu, J., Liang, B., Zou, X.-y., and Cheng, J.-c., 2016, "Broadband non-reciprocal transmission of sound with invariant frequency," Scientific reports, 6, p. 19824.
- [36] Popa, B.-I., and Cummer, S. A., 2014, "Non-reciprocal and highly nonlinear active acoustic metamaterials," Nature communications, 5, p. 3398.
- [37] Darabi, A., Fang, L., Mojahed, A., Fronk, M. D., Vakakis, A. F., and Leamy, M. J., 2019, "Broadband passive nonlinear acoustic diode," Physical Review B, 99(21), p. 214305.
- [38] Li, N., and Ren, J., 2014, "Non-reciprocal geometric wave diode by engineering asymmetric shapes of nonlinear materials," Scientific reports, 4, p. 6228.
- [39] Hussein, M. I., Leamy, M. J., and Ruzzene, M., 2014, "Dynamics of phononic materials and structures: Historical origins, recent progress, and future outlook," Applied Mechanics Reviews, 66(4), p. 040802.
- [40] Narisetti, R. K., Leamy, M. J., and Ruzzene, M., 2010, "A perturbation approach for predicting wave propagation in one-dimensional nonlinear periodic structures," Journal of Vibration and Acoustics, 132(3), p. 031001.
- [41] Blanchard, A., Sapsis, T. P., and Vakakis, A. F., 2018, "Non-reciprocity in nonlinear elastodynamics," Journal of Sound and Vibration, 412, pp. 326-335.
- [42] Shaw, S., and Pierre, C., 1991, "Non-linear normal modes and invariant manifolds," Journal of sound and Vibration, 150(1), pp. 170-173.

[43] Kerschen, G., Peeters, M., Golinval, J.-C., and Vakakis, A. F., 2009, "Nonlinear normal modes, Part I: A useful framework for the structural dynamicist," Mechanical Systems and Signal Processing, 23(1), pp. 170-194.

[44] Peeters, M., Viguié, R., Sérandour, G., Kerschen, G., and Golinval, J.-C., 2009, "Nonlinear normal modes, Part II: Toward a practical computation using numerical continuation techniques," Mechanical systems and signal processing, 23(1), pp. 195-216.